

# Stabilizing 3D EPI time series by servo navigation and phase equalization exploiting repeated shots (PEERS)

Malte Riedel<sup>1,\*</sup>, Thomas Ulrich<sup>1</sup>, Samuel Bianchi<sup>1</sup>, Klaas P. Pruessmann<sup>1</sup>

**1** Institute for Biomedical Engineering, ETH Zurich and University of Zurich, Switzerland

\* Corresponding author:

**Name** Dr. Malte Riedel

**Department** Institute for Biomedical Engineering

**Institute** ETH Zurich and University of Zurich

**Address** Gloriastrasse 35

8092 Zurich

Switzerland

**E-mail** malteriedel@mailbox.org

---

## Abstract

**Purpose:** To enable run-time head motion control and robust frequency corrections for 3D EPI fMRI.

**Methods:** A short 3D orbital navigator (3 ms) is inserted into a 3D EPI sequence. A linear perturbation model is calibrated to estimate rigid motion and frequency parameters per shot. Rigid motion is corrected by scan geometry updates in run-time, while several techniques are investigated to stabilize navigator-based frequency corrections in the reconstruction. An additional method termed PEERS is proposed that exploits the repetitive structure of fMRI scans to fine-tune shot-wise phase and frequency estimates using the motion-corrected EPI data itself.

**Results:** Servo navigation effectively reduces motion in the raw data of in-vivo fMRI scans in six subjects. PEERS provides high-precision frequency parameters for robust phase-corrected reconstructions in the phantom and in-vivo accounting for scanner drifts and slice encoding-related effects on EPI. In combination, servo navigation and PEERS achieve successful intra-volume corrections and consistent tSNR improvements of 8% on average throughout the brain. The two methods prove to be highly synergetic.

**Conclusion:** Servo navigation achieves high-precision motion correction for 3D-EPI fMRI in run-time and, in synergy with PEERS, provides stable frequency corrections with short navigators even for long echo times. With its automatic self-calibration and no hardware requirements, servo navigation and PEERS enable effective plug-and-play motion correction for 3D fMRI.

**Keywords:** fMRI, head motion, motion correction, field correction, EPI, feedback control, orbital navigators

---

## Introduction

Functional magnetic resonance imaging (fMRI) requires fast volume acquisitions to resolve the small signal variations of the BOLD contrast (1; 2; 3) in space and time. Due to its fast sampling and inherent robustness, two-dimensional echo-planar imaging (2D EPI) (4) has become a standard technique for fMRI acquisitions. However, 3D EPI offers intrinsically higher sensitivity and more benign spin history-related motion artifacts than 2D EPI, but, at the same time, makes segmented volume acquisition more vulnerable to physiological noise (5; 6). Head motion and magnetic field variations during the scan contaminate the voxel time series and statistical data analysis, posing major challenges for fMRI with 3D EPI (7; 8).

In principle, head motion can be addressed by motion prevention, robust sampling, and motion correction (9; 10; 11). Although the rapidly sampled volume acquisitions in fMRI are already relatively robust to motion, inter-volume motion and intra-volume artifacts can still persist (6). Motion prevention techniques include bite bars (12), cushioning, sedation (13), or dedicated patient preparation (14), which come with varying costs, preparation steps, health risks and levels of effectiveness. In addition, a wide range of prospective and retrospective techniques have been proposed for head motion correction based on external sensor hardware (15; 16; 17; 18; 19), MR-based navigators (20; 21; 22; 23; 24; 25; 26; 27; 28; 29), or data-driven self-navigation (30; 31; 32; 33), which have been shown to effectively mitigate motion artifacts in various scan settings.

Navigator-based motion corrections offer high-precision motion tracking without the need for external hardware, but at the cost of sequence interference (10). Recently, methods using short navigators of a few milliseconds have been proposed (27; 29; 34), which can be easily inserted in standard fMRI sequences. The servo navigation method (29; 34) uses short ( $\approx 3$  ms) 3D orbital navigators combined with a lightweight self-calibrating linear model for motion estimation and run-time correction. Once implemented, such navigated sequences offer plug-and-play operation, making motion correction more accessible for a wide range of studies.

In addition to head motion, magnetic field fluctuations are another confounding factor in voxel time series (35; 36; 37). The causes, the spatial complexity, and the time evolution of field variations are manyfold, including, for example, breathing (38; 39), pose-dependent field changes (10; 40; 41), scanner drift or sampling-related eddy currents (42; 43). Again, sensing mechanisms include external hardware (44; 45; 46; 47; 48; 49; 50) or MR navigators (28; 29; 34; 51; 52; 53) and data-driven techniques (52) and can be addressed in the reconstruction or in run-time.

---

In this work, servo navigation (29; 34) is integrated into a segmented 3D EPI sequence for run-time motion and frequency correction in fMRI. The frequency precision proves to be critical for robust EPI phase correction at the long echo times used in fMRI and requires dedicated handling. An EPI-based self-correction termed phase equalization exploiting repeated shots (PEERS) is proposed to fine-tune the frequency and phase estimation, leveraging the redundancy in the repetitive structure of fMRI sequences. Motion correction becomes a fundamental element to maintain the comparability over the volume repetitions for high-precision frequency estimation by PEERS, and PEERS, in return, reduces the burden on the navigator frequency precision. Phantom and in-vivo fMRI scans are performed with and without motion to study the individual and synergistic performance of servo navigation and PEERS.

## Methods

### Servo navigation for segmented 3D EPI

The concept of servo navigation has previously been studied for 3D gradient echo imaging (29; 34) and is, in this work, integrated into a segmented 3D EPI sequence. The sequence diagram is shown in Fig. 1A and consists of a slab-selective excitation (Ex) and an EPI readout. In each EPI shot, the sequence blips through the phase encoding dimension (P), while applying varying prephasers and rephasers in the slice encoding dimension (S) from shot to shot. By this, one k-space plane is acquired per shot with repetition time  $T_R$  yielding a full volume after  $N_z$  slice encodings with volume acquisition time  $T_{vol} = T_R * N_z$ .

Servo navigation (29; 34) requires three basic components (Fig. 1B): a navigator, a model for parameter estimation, and a mechanism for run-time scan control. First, a 3D orbital navigator, acquiring orbits around three orthogonal axes sequentially at a k-space radius of 400 rad/m, is inserted between the excitation and the EPI as shown in Fig. 1A. The duration of the navigator  $T_{nav}$  can be varied and is, by default, set to 3.2 ms. Second, a linear model is calibrated on the fly using a finite difference approach (29) after a sub-second acquisition of reference navigators. The linear model  $M$  (29) relates the parameter vector  $\vec{\Delta}$  to the complex-valued signal variations from a reference navigator signal vector  $\vec{s}^{(0)}$ :

$$\vec{s}(\vec{\Delta}) - \vec{s}^{(0)} = M\vec{\Delta}, \quad [1]$$

where  $\vec{s}(\vec{\Delta})$  is the current navigator signal vector and  $\vec{\Delta}$  includes six 3D rigid motion parameters, a

---

global phase  $\Delta\phi$  and a global frequency parameter  $\Delta\omega$ . Finally, a control mechanism is implemented to adapt the scan geometry by rotating the gradients and shifting the slab-selective excitation in run-time. This process forms a control loop that stabilizes navigator acquisitions and, by this, keeps the model intact beyond the initial linear range.

### Navigator-based phase correction

The incremental update parameters for global phase  $\Delta\phi$  and frequency  $\Delta\omega$  from the navigator are accumulated over the scan as described in Ref. (29) yielding parameter time courses for the total global phase  $\Delta\phi_{total,j}$  and the frequency  $\Delta\omega_{total,j}$  with the shot index  $j$ . A navigator-based phase correction  $\Delta\varphi_j(t)$  can be applied to the EPI k-space data in the reconstruction by:

$$\Delta\varphi_j(t) = \Delta\omega_{corr,j} t + \Delta\phi_{corr,j}, \quad [2]$$

where  $t$  is the intra-shot acquisition time of the samples along the EPI train.  $\Delta\omega_{corr,j}$  and  $\Delta\phi_{corr,j}$  are the navigator traces for the total global phase and frequency after optional filtering over time:

$$\Delta\phi_{corr,j} = \text{filter}(\Delta\phi_{total,j}), \quad [3]$$

$$\Delta\omega_{corr,j} = \text{filter}(\Delta\omega_{total,j}). \quad [4]$$

The phase correction in Eq. 2 is, however, prone to noise amplification for long echo times or sampling durations, because the noise in the frequency parameter  $\Delta\omega_{corr,j}$  is amplified linearly with the acquisition time  $t$ . Requirements for field parameter precisions, therefore, depend on the sequence timing. Noise amplification can be reduced by filtering the field parameters, which usually reduces the effective bandwidth of the signal, or by prolonging the navigator acquisition time  $T_{nav}$  to increase the field sensitivity and SNR at the cost of reduced sampling efficiency and flexibility.

As an alternative strategy, a phase correction with relative timing is proposed to suppress noise amplification for short volume acquisitions:

$$\Delta\varphi_j^{rel}(t) = \Delta\varphi_j(t - T_E) = \Delta\omega_{corr,j} (t - T_E) + \Delta\phi_{corr,j}, \quad [5]$$

Here, the phase correction is performed with timing  $t_{rel} = (t - T_E)$  relative to the echo time  $T_E$  and neglects the shot-wise phases  $\Delta\omega_{corr,j} T_E$  within a volume acquisition. By this, the phase along the k-space line  $(0, 0, k_z)^T$  remains unchanged. Relative timing is beneficial if the frequency variation of  $\Delta\omega_{corr,j}$  within a volume acquisition is dominated by noise rather than by the actual field evolution, which is usually the case for fast fMRI volume acquisitions of a few seconds at 3T.

---

## EPI-based phase correction using PEERS

fMRI scans possess a strongly repetitive structure with only minor BOLD-induced contrast variations that can be leveraged to perform frequency and phase self-corrections based on the EPI signal itself. The proposed technique is termed phase equalization exploiting repeated shots (PEERS). An overview of the algorithm is shown in Fig. 2. Global frequency and phase parameters are calculated for each shot by exploiting redundancies in repetitive fMRI scans and comparing each echo to its corresponding peer in the reference volume. Each shot index  $j$  is associated with an index triple  $(d, \kappa_z, \kappa_y)$  including volume repetition index  $d$ , and slice and phase encoding indices  $\kappa_z$  and  $\kappa_y$ :

1. If  $d = 1$  (first volume repetition), set reference echoes  $s_{\text{ref}, \kappa_z, \kappa_y} = s_{1, \kappa_z, \kappa_y}$ .
2. else ( $d > 1$ ):
  - (a) Calculate relative phase  $\Delta\varphi_{d, \kappa_z, \kappa_y} = \angle(s_{\text{ref}, \kappa_z, \kappa_y}^H s_{d, \kappa_z, \kappa_y})$  for each echo  $(d, \kappa_z, \kappa_y)$ ,
  - (b) Unwrap phase  $\Delta\varphi_{d, \kappa_z, \kappa_y}$  along echo train  $(\kappa_y)$ ,
  - (c) Perform shot-wise first-order phase fit along echo train  $(\kappa_y)$ ,
  - (d) Extract frequency  $\Delta\omega_{\text{epi}, j}$  (slope) and phase  $\Delta\phi_{\text{epi}, j}$  (offset) from the fit,
  - (e) Perform EPI signal phase correction by  $\Delta\varphi_{\text{epi}, j}(t) = \Delta\omega_{\text{epi}, j} t + \Delta\phi_{\text{epi}, j}$ .

PEERS reduces the phase variations to the first order with respect to the reference volume and, by this, basically matches the frequency- and phase-induced point spread function of all volume repetitions, leading to stabilized voxel time series. Unaware of the causes of the parameter variations, the correction includes both system- and physiology-related effects like field changes, RF phase drifts, and breathing. The sensitivity of the EPI sampling to frequency variations increases with  $T_E$  in the same way as the precision requirements, making the correction naturally robust against variations in echo time, sampling duration, and field strength. The technique is generally independent of the slice encoding order.

## Acquisition details

A scan protocol consisted of three 3D EPI runs lasting 10 min each: (i) without PMC ( $T_{\text{nav}} = 3.2$  ms), (ii) with PMC ( $T_{\text{nav}} = 3.2$  ms), and (iii) with PMC and a long navigator ( $T_{\text{nav}} = 11.5$  ms). For case (iii), the navigator was stretched in time with the same trajectory and keeping the same number of samples. The order of the three runs was randomized and unknown to the subject.

---

The scan parameters were: 2.5 mm isotropic resolution, FOV= $230 \times 200 \times 140 \text{ mm}^3$  (incl. 1.4-fold slice oversampling),  $N_z = 32$  slice encoding steps with linear ordering, reduction factors  $2.2 \times 1.75$  (phase  $\times$  slice), flip angle=17.2 deg, TE=30 ms,  $T_R=64 \text{ ms}$ ,  $T_{vol}=2.0 \text{ s}$ , and 300 volumes after 10 initial dummy volumes to build up the steady state. SPIR (54) was used for fat suppression. A T1-weighted scan was acquired at isotropic resolution 1.1 mm for anatomical reference.

The method was evaluated in a phantom and in-vivo with a visuomotor task. For the phantom experiments, a sphere filled with small PMMA spheres and a copper sulfate solution was used as described in Ref. (29). In-vivo, the scan sets were performed in six healthy volunteers in accordance with local ethical regulations on a 3T Philips (Best, The Netherlands) Ingenia scanner with a vendor-provided 32-channel head coil. The fMRI task consisted of images with arrows in the upper or lower visual field using a fully randomized, event-related design. Subjects were asked to press the left or right button according to the displayed arrows. Respiratory and cardiac physiology was monitored using a breathing belt and a pulse oximeter.

To study the influence of motion, two of the six subjects were instructed to repeat a succession of rotations starting from a reference position and approximately changing pose every 10 sec to  $[0, +1^\circ(p), 0, -1^\circ(p), 0, +1^\circ(y), 0, -1^\circ(y)]$  with  $p$  and  $y$  being pitch (nod) and yaw (head shake) rotations. The subjects saw a clock on the screen. The scans were performed with and without PMC in shortened 3-min runs (100 volume repetitions).

## Reconstruction details

The image reconstruction was implemented in MATLAB (MathWorks Inc., Natick, MA, USA) using the pipeline of ReconFrame (Gyrotools, Zurich, Switzerland) with several modifications. After some basic vendor-specific corrections, the k-space data is corrected for the global phase and frequency parameters from the navigators' run-time estimates following the descriptions in Section 2.2. A non-causal median filter of size 9 (approx. 0.6 s) is used for filtering. After gridding of the EPI ramp samples, the k-space data is corrected for shifts in measurement and phase direction according to the navigators' run-time shift estimates. This is done in the reconstruction, because only the slab shift is treated in run-time by the scanner.

Next, EPI-based PEERS corrections are performed from shot-wise phase and frequency estimates, as discussed in Section 2.3. A Nyquist ghosting correction was calculated from a vendor-provided pre-scan and applied in hybrid space followed by a ReconFrame implementation of regularized SENSE (55) in image space. All navigator-based corrections are turned off if the PMC is

---

disabled. Sensitivity maps were reconstructed from the vendor’s reference scan in the beginning of the scan set and included masking and smoothing.

Statistical analysis was performed using SPM12 (56), including volume realignment, structural image co-registration, and tissue segmentation into gray and white matter, CSF, skull, soft tissue, and background. Physiological traces from the breathing belt and pulse oximeter were processed using PhysIO (57) and included as regressors in the generalized linear model. tSNR was calculated before and after SPM volume realignment as the voxel-wise mean over time divided by the voxel-wise standard deviation (std) over time:  $\text{tSNR}_{\mathbf{r}} = \text{mean}_{\nu}(\rho_{\mathbf{r},\nu}) / \text{std}_{\tau}(\rho_{\mathbf{r},\nu})$ , where  $\rho_{\mathbf{r},\nu}$  is the magnitude signal of a voxel at location  $\mathbf{r}$  and volume (time) index  $\nu$ .

## Results

### Run-time motion correction example

Figure 3 shows an in-vivo example with instructed motion for *PMC off* and *PMC on* comparing mean and standard deviation (std) of the voxel time series as well as the realignment parameters. For *PMC off*, the central slice of the mean volume appears blurred, while the standard deviation shows strongly enhanced edges and choppy patterns throughout the brain in the logarithmic image. In contrast, the blurring is mitigated by *PMC on*, and the imprint of anatomical features and choppy patterns in the standard deviation images is clearly reduced. The edge enhancement mainly originates from frequency-induced EPI shifting that is corrected by servo navigation, whereas choppy patterns are caused by motion-induced inconsistencies.

The volume realignment parameters for *PMC off* show the instructed motion pattern of successive pitch and yaw rotations, which are left uncorrected in the data. For *PMC on*, the volume realignment detects only minor motions close to zero that are left after the run-time motion correction. However, the onset of the motion events is still visible with *PMC on* by small spikes and plateaus, especially for the pitch rotation (purple).

### Realignment parameter statistics

Figure 4 shows the volume realignment parameter statistics and RMSE results for the data from all subjects without instructed motion for *PMC off* (black boxes) and *PMC on* (green boxes). RMSE, median realignment parameters, and inter-quartile ranges (heights of the boxes) are consistently reduced by the PMC for all parameters. The RL shift includes not only involuntary shifts from the



---

subjects but also the EPI shifting in phase encoding direction due to frequency drifts as the volume realignment is incapable of differentiating between the two. As the navigator corrects both for subject- and frequency-induced shifts in phase encoding direction, the RL shift is most prominently reduced.

### PEERS phase correction example

Figure 5 shows PEERS corrections in the phantom without PMC. The mean of the voxel time series is shown for reference. Without PEERS, the standard deviation (std) is the highest and is strongly reduced by realignment. With PEERS, the standard deviation is further reduced and realignment does not give an additional advantage. PEERS captures a frequency drift of about 5 Hz/min (B), and the parameters also show patterns that repeat with volume acquisition time  $T_{vol}$  (C).

In these scans, continuous frequency drift is the major cause of tSNR instability, which appears as EPI shifting in the low-bandwidth phase encoding direction. Volume realignment is well suited to correct for these inter-volume shifts, strongly reducing the standard deviation for *PEERS off*. While realignment can only correct for global transformations between volumes, PEERS is capable of addressing both inter- and intra-volume phase and frequency variations including effects from slow frequency drifts, but also from sampling-related effects (see Figs. 5B and C). By this, PEERS reduces the respective artifacts, and thus improves volume consistency.

### Spectral analysis of PEERS parameters

Figure 6 shows the power spectra of the PEERS parameters compared to the respective navigator spectra. The PEERS parameters contain a Dirac-comp pattern spaced by  $f_{vol} = 1/T_{vol} \approx 0.49$  Hz that is not visible for the navigator parameters and is associated with the repetitive  $T_{vol}$ -spaced patterns of the time domain signals in Fig. 5C. The patterns thus match the frequency of the slice encoding, indicating that the EPI data is affected by transient field effects, which are not seen and, therefore, also not correctable by the navigator in the beginning of the sequence.

### In-vivo example of tSNR improvements

Figure 7 compares the tSNR in-vivo with and without PMC, PEERS and volume realignment. The worst tSNR performance appears when all options are disabled. By enabling the individual corrections one by one, tSNR improves consistently, showing the best result with all corrections enabled. If both PMC and PEERS are enabled, volume realignment can still improve the results,

---

albeit only slightly. Note that *PMC off* and *PMC on* are always two separate datasets and could be affected by different underlying motions, whereas PEERS, as a pure reconstruction technique, can be switched off and on for the exact same raw data.

### In-vivo tSNR statistics

Table 1 shows the mean tSNR over all subjects for different segmented anatomies after realignment including gray matter (GM), white matter (WM), cerebrospinal fluid (CSF), and their combination (Whole brain). *Whole brain - not aligned* is given as a reference before realignment.

Without realignment, PEERS only shows minor improvements in tSNR ( $< 3\%$ ) compared to PMC with (41%). Together, PMC and PEERS achieve an overall whole brain tSNR increase of 54%. The main tSNR degradation factor that is corrected here is the frequency drift. If realignment is performed, PEERS consistently improves tSNR for all anatomies and the improvements for PEERS are larger than for PMC. PMC alone may even show local tSNR losses as in white matter, but combined with PEERS, the PMC-induced tSNR losses are removed. Note that these scans were conducted without motion instructions and included only experienced healthy volunteers. Therefore, motion-induced intra-volume disturbances were rather small, leaving more room for corrections of sampling-induced disturbances by PEERS than for the PMC. The best tSNR performance is achieved using all three methods: PMC, PEERS and realignment.

### Synergy of PMC and PEERS

Figure 8 shows a tSNR comparison for an in-vivo case with instructed motion after realignment. With motion, the mean tSNR drops from about 50 (a; reference) to 39 (c). The mean tSNR increases to 42 for PEERS alone (d) and to 44 for PMC alone (e), while it increases to 49 for both corrections (f). Still, the corrected motion case does not achieve the tSNR performance of 63 of the motion-free case with PEERS. If motion is present, the relative importance thus of the PMC corrections increases with respect to PEERS.

### Frequency precision considerations

Figure 9 characterizes the navigator’s frequency precision, its impact on tSNR and various ways to mitigate noise propagation into the phase correction including also PEERS. In (A), the standard deviation of the (unfiltered) frequency  $\Delta\omega_{total}$  is plotted for different navigator durations  $T_{nav}$  for

---

phantom and in-vivo scans. The frequency precision grows approximately linearly with the duration of sampling.  $1/T_{nav}$ -guidance lines starting from the first 2.3ms-navigator value are given to visualize the trend. tSNR maps for navigator durations of 3.2ms and 11.5ms with and without PEERS are shown in Fig. 9B. Phase corrections with unfiltered frequency  $\Delta\omega_{total}$  from short navigators result in poor tSNR, which is improved by longer navigators due to the increased precision. As shown in (C), phase corrections with filtered frequencies  $\Delta\omega_{corr}$  (Eqs. 3-4) and with relative timing  $t_{rel}$  (Eq. 5) considerably improve tSNR also for short 3.2ms-navigators. Nevertheless, EPI-based PEERS corrections, which rely on the repetitive sequence structure, outperform navigator corrections in all cases.

## Discussion

In this work, servo navigation has been successfully integrated into a segmented 3D EPI sequence for run-time motion corrected fMRI. The method does not impose additional steps in the MR workflow, offering on-the-fly self-calibration without additional hardware. The shot-wise intra-volume corrections of servo navigation mitigate motion both between volumes and within each volume, and by this improves the stability of voxel time series beyond rigid realignment. Various methods to reduce noise propagation from the navigator’s frequency estimates into the EPI phase corrections have been investigated to enable frequency-corrected servo navigation. In addition, PEERS has been shown to offer robust shot-wise phase and frequency corrections based on the EPI data itself by exploiting redundancies in motion-corrected repetitive sequences. The stabilized frequency corrections by PEERS enable servo navigation with short 3.2ms-navigators even for fMRI sequences with long echo times underlining the synergistic relationship of the two corrections.

### Servo navigation for 3D EPI

In Figs. 3-4, servo navigation has been shown to capture motion and frequency drifts well, significantly reducing the amount of motion in the imaging raw data. Nevertheless, residual motion has been noticed even with PMC correction in the form of remaining spikes at the onsets of instructed pitch rotations and small plateaus while the position was held. The onset spikes are probably caused by the latency of the control system (15), as our PMC implementation requires about 300ms to apply an estimated motion state. The small plateaus in the pitch-rotated positions could be caused by secondary motion effects like pose-induced coil sensitivity or field changes (10), which can induce

---

parameter biases (34). Navigator signal variations from coil sensitivity changes should generally be present for both instructed rotations, while only nodding rotations are related to susceptibility-induced field changes (40). As the plateaus are mainly seen for nodding, the biases are probably related to parameter biases from pose-dependent field changes.

It is important to note that the volume realignment, which serves as a reference for motion quantification in this study, is also biased by pose-dependent contrast variations, such as varying distortions or signal dropouts around the nasal cavities after pose changes. Volume realignment itself even benefits from the PMC, because the registered volumes are more consistent, and updating the phase encoding direction in run-time reduces geometric distortions.

### **Phase matching by PEERS**

PEERS has been shown to detect and correct frequency drifts and slice encoding-related sampling effects (Figs. 5-6). The latter are probably caused by long-term eddy currents that are generated by the slice encoding pre-phasers directly prior to the EPI readout. As PEERS is restricted to a first-order phase fit over the echo train, it can handle only frequency offsets that are constant over the echo train as from long-term eddy currents. More high-frequent variations, e.g. from vibrations or short-term eddy currents, cannot be modeled in this way, but were also not observed in the data.

The signal stability improvements by PEERS have been found on two different scanners of the same vendor in our lab. As the parameter fits are related to sampling-specific scanner imperfections, the relevance of this correction might depend on the vendor platform and the specific system used. However, slice encoding-induced eddy currents are expected to be present on other vendor platforms as well. For clarification, a cross-vendor evaluation is necessary.

Note that the PEERS method has certain similarities with a self-navigation approach for 3D multishot EPI published by Moeller et al. (58). This method also exploits the repetitiveness of a diffusion sequence with multiple diffusion directions and encoding strengths to derive shot-wise phase navigators. However, in the diffusion case, the phase navigators need to be spatially resolved, resulting in higher computational demands and a more complex phase-fitting procedure, which is probably more prone to instabilities compared to the proposed first-order phase model with only two parameter per shot.

---

## Synergy of servo navigation and PEERS

It is noteworthy that the shot-wise phase equalization crucially depends on the comparability between the current and its peer, the reference shot. This is only given if motion correction (either in run-time or in retrospect) is applied before the PEERS estimation, and thus the k-space signal remains in its place unaffected by rotations. The relative phase calculation, which is based on the complex-valued scalar product between the echo signals, would otherwise mix unrelated k-space locations. Although PEERS has been shown to improve tSNR even without PMC both in-vivo (Fig. 7) and in the phantom (Fig. 5), motion generally makes the method prone to errors that could even corrupt image reconstruction if uncorrected.

At the same time, PEERS alleviates frequency precision requirements on the servo navigation method by fine-tuning the frequency parameters using the EPI data. In this way, the techniques enable intra-volume frequency corrections for long echo times even with short 3.2ms-navigator acquisitions. In addition, the navigator-based frequency and phase correction prior to PEERS is still beneficial, because it keeps the signal phases close to each other and avoids problems in the non-linear phase unwrapping step of PEERS. At the same time, EPI-based corrections avoid potential phase and frequency biases imposed by the navigator sensing, which could stem from mismatches of their respective transient eddy current and vibration characteristics.

The combination of servo navigation and PEERS has been shown to consistently improve tSNR by about 8% in the fMRI study, even without instructed motion, in experienced volunteers, with short 2 sec-volume acquisitions and including realignment. Without realignment, tSNR is increased by 54% (Tab. 1). For instructed motion (Fig. 8), the tSNR was improved by 5 – 10% for each individual method, while together achieving a 26% tSNR increase on average throughout the whole brain. Besides servo navigation as a specific kind of PMC, PEERS can also be combined with other prospective and retrospective motion correction techniques that maintain the signal correspondence in k-space prior to the correction. In addition, PEERS can also be used to correct scans that involve signal averaging, which also represents highly repetitive acquisitions.

## Field precision considerations

Navigator frequency precision was found to increase approximately linear with sampling duration (Fig. 9). Longer navigator acquisitions therefore reduce noise in the frequency parameters and stabilize the associated phase corrections at the cost of reduced time efficiency of the main imaging

---

sequence. Parameter filtering has also been shown to effectively reduce noise in phase corrections but usually reduces the correction bandwidth at the same time. Correcting with relative timing  $t_{rel}$  (Eq. 5) leaves both the navigator sampling burden and the correction bandwidth unchanged. The technique omits bulk phases from frequency variations during the volume sampling, which was found to be effective for short 2sec-volume samplings but inappropriate for long volume acquisitions with frequency variations as in Ref. (34).

In a previous study (34), the servo navigation has been extended to run-time gradient shimming by calibrating and updating three more gradient shim parameters in the model. Due to the complexity of the frequency corrections studied here, the model has been restricted to zeroth-order field corrections in this work. First- and higher-order dynamic shimming are subject to future work. Similar to the frequency estimation, uncontrolled noise in the navigator parameter estimates is expected to harm stability for higher-order corrections at long echo times, and field sensitivity is expected to increase with navigator duration.

## Future research

3D EPI has been shown to offer greater flexibility and sensitivity for high-resolution fMRI, but is more sensitive to physiological noise and scanner system imperfections due to the segmented volume acquisitions (5). The combination of servo navigation and PEERS reduces the sensitivity of 3D EPI to physiological and sampling-related effects. Therefore, the relative comparison of 2D and 3D fMRI is a focus of future projects.

In addition, servo navigation and PEERS have been tested in six healthy and experienced volunteers in this study with a technical focus on enhancements in the imaging stability measured by tSNR. However, it is not yet clear what impact these findings have on the extraction of functional activity and connectivity from the fMRI data. To investigate their true impact, future studies involve evaluating these methods with dedicated study designs and data analysis pipelines in larger cohorts.

## Acknowledgments

This work has received funding from the European Union’s Horizon 2020 research and innovation program under grant agreement No. 885876 (AROMA project). In addition, the technical and research support from Philips Healthcare is gratefully acknowledged.

---

## References

- [1] Ogawa S, Tank D W, Menon R, et al. Intrinsic signal changes accompanying sensory stimulation: functional brain mapping with magnetic resonance imaging.. *Proceedings of the National Academy of Sciences*. 1992;89(13):5951–5955.
- [2] Ogawa S., Menon R.S., Tank D.W., et al. Functional brain mapping by blood oxygenation level-dependent contrast magnetic resonance imaging. A comparison of signal characteristics with a biophysical model. *Biophysical Journal*. 1993;64(3):803–812.
- [3] Belliveau J. W., Kennedy D. N., McKinsty R. C., et al. Functional Mapping of the Human Visual Cortex by Magnetic Resonance Imaging. *Science*. 1991;254(5032):716–719.
- [4] Mansfield P. Multi-planar image formation using NMR spin echoes. *Journal of Physics C: Solid State Physics*. 1977;10(3):L55–L58. Number: 3.
- [5] Poser B.A., Koopmans P.J., Witzel T., Wald L.L., Barth M.. Three dimensional echo-planar imaging at 7 Tesla. *NeuroImage*. 2010;51(1):261–266.
- [6] Zaitsev Maxim, Akin Burak, LeVan Pierre, Knowles Benjamin R.. Prospective motion correction in functional MRI. *NeuroImage*. 2017;154:33–42.
- [7] Van Dijk Koene R.A., Sabuncu Mert R., Buckner Randy L.. The influence of head motion on intrinsic functional connectivity MRI. *NeuroImage*. 2012;59(1):431–438.
- [8] Liu Thomas T.. Noise contributions to the fMRI signal: An overview. *NeuroImage*. 2016;143:141–151.
- [9] Zaitsev Maxim, Maclaren Julian, Herbst Michael. Motion artifacts in MRI: A complex problem with many partial solutions: Motion Artifacts and Correction. *Journal of Magnetic Resonance Imaging*. 2015;42(4):887–901.
- [10] Maclaren Julian, Herbst Michael, Speck Oliver, Zaitsev Maxim. Prospective motion correction in brain imaging: A review. *Magnetic Resonance in Medicine*. 2013;69(3):621–636.
- [11] Godenschweger F, Kägebein U, Stucht D, et al. Motion correction in MRI of the brain. *Physics in Medicine and Biology*. 2016;61(5):R32–R56.

- 
- [12] Menon V., Lim K. O., Anderson J. H., Johnson J., Pfefferbaum A.. Design and efficacy of a head-coil bite bar for reducing movement-related artifacts during functional MRI scanning. *Behavior Research Methods, Instruments, & Computers*. 1997;29(4):589–594.
- [13] Bernal . fMRI Under Sedation: What Is the Best Choice in Children?. *Journal of Clinical Medicine Research*. 2012;.
- [14] De Bie Henrica M. A., Boersma Maria, Wattjes Mike P., et al. Preparing children with a mock scanner training protocol results in high quality structural and functional MRI scans. *European Journal of Pediatrics*. 2010;169(9):1079–1085.
- [15] Zaitsev M., Dold C., Sakas G., Hennig J., Speck O.. Magnetic resonance imaging of freely moving objects: prospective real-time motion correction using an external optical motion tracking system. *NeuroImage*. 2006;31(3):1038–1050.
- [16] Ooi Melvyn B, Krueger Sascha, Thomas William J, Swaminathan Srirama V, Brown Truman R. Prospective real-time correction for arbitrary head motion using active markers. *Magnetic Resonance in Medicine*. 2009;62(4):943–954.
- [17] Haeberlin Maximilian, Kasper Lars, Barmet Christoph, et al. Real-time motion correction using gradient tones and head-mounted NMR field probes. *Magnetic Resonance in Medicine*. 2015;74(3):647–660.
- [18] Schildknecht Christoph Michael, Brunner David Otto, Schmid Thomas, Reber Jonas, Marjanovic Josip, Pruessmann Klaas P. Wireless motion tracking with short-wave radiofrequency. *Proceedings of the 27th International Society of Magnetic Resonance in Medicine, Montreal, Canada*. 2019;27:66.
- [19] Niekerk Adam, Kouwe Andre, Meintjes Ernesta. Toward “plug and play” prospective motion correction for MRI by combining observations of the time varying gradient and static vector fields. *Magnetic Resonance in Medicine*. 2019;82(3):1214–1228.
- [20] Ehman Richard L., Felmlee Joel P.. Adaptive technique for high-definition MR imaging of moving structures.. *Radiology*. 1989;173(1):255–263.
- [21] Fu Zhuo Wu, Wang Yi, Grimm Roger C., et al. Orbital navigator echoes for motion measurements in magnetic resonance imaging. *Magnetic Resonance in Medicine*. 1995;34(5):746–753.



- 
- [22] Welch Edward Brian, Manduca Armando, Grimm Roger C., Ward Heidi A., Jack Jr. Clifford R.. Spherical navigator echoes for full 3D rigid body motion measurement in MRI. *Magnetic Resonance in Medicine*. 2002;47(1):32–41.
- [23] Kouwe André J.W., Benner Thomas, Dale Anders M.. Real-time rigid body motion correction and shimming using cloverleaf navigators. *Magnetic Resonance in Medicine*. 2006;56(5):1019–1032.
- [24] White Nathan, Roddey Cooper, Shankaranarayanan Ajit, et al. PROMO: Real-time prospective motion correction in MRI using image-based tracking. *Magnetic Resonance in Medicine*. 2010;63(1):91–105.
- [25] Kober Tobias, Marques José P., Gruetter Rolf, Krueger Gunnar. Head motion detection using FID navigators. *Magnetic Resonance in Medicine*. 2011;66(1):135–143.
- [26] Skare Stefan, Hartwig Axel, Mårtensson Magnus, Avventi Enrico, Engström Mathias. Properties of a 2D fat navigator for prospective image domain correction of nodding motion in brain MRI: 2D FatNav for Motion Correction in Brain MRI. *Magnetic Resonance in Medicine*. 2015;73(3):1110–1119.
- [27] Wallace Tess E., Afacan Onur, Waszak Maryna, Kober Tobias, Warfield Simon K.. Head motion measurement and correction using FID navigators. *Magnetic Resonance in Medicine*. 2019;81(1):258–274.
- [28] Liu Jiaen, Gelderen Peter, Zwart Jacco A., Duyn Jeff H.. Reducing motion sensitivity in 3D high-resolution T2\*-weighted MRI by navigator-based motion and nonlinear magnetic field correction. *NeuroImage*. 2020;206:116332.
- [29] Ulrich Thomas, Riedel Malte, Pruessmann Klaas P. Servo navigators: Linear regression and feedback control for rigid-body motion correction. *Magnetic Resonance in Medicine*. 2024;91(5):1876–1892.
- [30] Atkinson D., Hill D.L.G., Stoyke P.N.R., Summers P.E., Keevil S.F.. Automatic correction of motion artifacts in magnetic resonance images using an entropy focus criterion. *IEEE Transactions on Medical Imaging*. 1997;16(6):903–910.
- [31] Bammer Roland, Aksoy Murat, Liu Chunlei. Augmented generalized SENSE reconstruction to correct for rigid body motion. *Magnetic Resonance in Medicine*. 2007;57(1):90–102.

- 
- [32] Loktyushin Alexander, Nickisch Hannes, Pohmann Rolf, Schölkopf Bernhard. Blind retrospective motion correction of MR images: Blind Retrospective Motion Correction. *Magnetic Resonance in Medicine*. 2013;70(6):1608–1618.
- [33] Polak Daniel, Splitthoff Daniel Nicolas, Clifford Bryan, et al. Scout accelerated motion estimation and reduction (SAMER). *Magnetic resonance in medicine*. 2022;87(1):163–178.
- [34] Riedel Malte, Ulrich Thomas, Pruessmann Klaas P.. Run-time motion and first-order shim control by expanded servo navigation. *Magnetic Resonance in Medicine*. 2025;93(1):166–182. \_eprint: <https://onlinelibrary.wiley.com/doi/pdf/10.1002/mrm.30262>.
- [35] Koch Kevin M., Rothman Douglas L., De Graaf Robin A.. Optimization of static magnetic field homogeneity in the human and animal brain in vivo. *Progress in Nuclear Magnetic Resonance Spectroscopy*. 2009;54(2):69–96.
- [36] Juchem Christoph, De Graaf Robin A.. B0 magnetic field homogeneity and shimming for in vivo magnetic resonance spectroscopy. *Analytical Biochemistry*. 2017;529:17–29.
- [37] Stockmann Jason P., Wald Lawrence L.. In vivo B 0 field shimming methods for MRI at 7 T. *NeuroImage*. 2018;168:71–87.
- [38] Raj Devesh, Paley Derek P, Anderson Adam W, Kennan Richard P, Gore John C. A model for susceptibility artefacts from respiration in functional echo-planar magnetic resonance imaging. *Physics in Medicine and Biology*. 2000;45(12):3809–3820.
- [39] Moortele Pierre-François, Pfeuffer Josef, Glover Gary H, Ugurbil Kamil, Hu Xiaoping. Respiration-induced B0 fluctuations and their spatial distribution in the human brain at 7 Tesla. *Magnetic Resonance in Medicine*. 2002;47(5):888–895.
- [40] Marques J.P., Bowtell R.. Application of a Fourier-based method for rapid calculation of field inhomogeneity due to spatial variation of magnetic susceptibility. *Concepts in Magnetic Resonance Part B: Magnetic Resonance Engineering*. 2005;25B(1):65–78.
- [41] Liu Jiaen, Zwart Jacco A., Gelderen Peter, Murphy-Boesch Joseph, Duyn Jeff H.. Effect of head motion on MRI B 0 field distribution: Liu et al.. *Magnetic Resonance in Medicine*. 2018;80(6):2538–2548.

- 
- [42] Boesch Ch., Gruetter R., Martin E.. Temporal and spatial analysis of fields generated by eddy currents in superconducting magnets: Optimization of corrections and quantitative characterization of magnet/gradient systems. *Magnetic Resonance in Medicine*. 1991;20(2):268–284.
  - [43] Vannesjo Signe J., Haeberlin Maximilan, Kasper Lars, et al. Gradient system characterization by impulse response measurements with a dynamic field camera. *Magnetic Resonance in Medicine*. 2013;69(2):583–593.
  - [44] Gelderen Peter, De Zwart JA, Starewicz P, Hinks RS, Duyn JH. Real-time shimming to compensate for respiration-induced B0 fluctuations. *Magnetic Resonance in Medicine*. 2007;57(2):362–368.
  - [45] Wilm Bertram J., Barmet Christoph, Pavan Matteo, Pruessmann Klaas P.. Higher order reconstruction for MRI in the presence of spatiotemporal field perturbations: Higher Order Reconstruction for MRI. *Magnetic Resonance in Medicine*. 2011;65(6):1690–1701.
  - [46] Kasper Lars, Bollmann Saskia, Vannesjo S. Johanna, et al. Monitoring, analysis, and correction of magnetic field fluctuations in echo planar imaging time series. *Magnetic Resonance in Medicine*. 2015;74(2):396–409.
  - [47] Duerst Yolanda, Wilm Bertram J., Wyss Michael, et al. Utility of real-time field control in T<sub>2</sub>\*-Weighted head MRI at 7T: Utility of Real-Time Field Control. *Magnetic Resonance in Medicine*. 2016;76(2):430–439.
  - [48] Kasper Lars, Engel Maria, Barmet Christoph, et al. Rapid anatomical brain imaging using spiral acquisition and an expanded signal model. *NeuroImage*. 2018;168:88–100.
  - [49] Engel Maria, Kasper Lars, Barmet Christoph, et al. Single-shot spiral imaging at 7 T. *Magnetic Resonance in Medicine*. 2018;80(5):1836–1846. Number: 5.
  - [50] Vionnet Laetitia, Aranovitch Alexander, Duerst Yolanda, et al. Simultaneous feedback control for joint field and motion correction in brain MRI. *NeuroImage*. 2021;226:117286.
  - [51] Wallace Tess E., Afacan Onur, Kober Tobias, Warfield Simon K.. Rapid measurement and correction of spatiotemporal B<sub>0</sub> field changes using FID navigators and a multi-channel reference image. *Magnetic Resonance in Medicine*. 2020;83(2):575–589.

- 
- [52] Splitthoff D.N., Zaitsev Maxim. SENSE shimming (SSH): A fast approach for determining  $B_0$  field inhomogeneities using sensitivity coding: SENSE Shimming (SSH). *Magnetic Resonance in Medicine*. 2009;62(5):1319–1325.
- [53] Wallace Tess E., Kober Tobias, Stockmann Jason P., Polimeni Jonathan R., Warfield Simon K., Afacan Onur. Real-time shimming with FID navigators. *Magnetic Resonance in Medicine*. 2022;88(6):2548–2563.
- [54] Kaldoudi Eleni, Williams Steve CR, Barker Gareth J, Tofts Paul S. A chemical shift selective inversion recovery sequence for fat-suppressed MRI: theory and experimental validation. *Magnetic resonance imaging*. 1993;11(3):341–355. Number: 3 Publisher: Elsevier.
- [55] Pruessmann Klaas P., Weiger Markus, Scheidegger Markus B., Boesiger Peter. SENSE: sensitivity encoding for fast MRI. *Magnetic Resonance in Medicine*. 1999;42(5):952–962.
- [56] Penny William D, Friston Karl J, Ashburner John T, Kiebel Stefan J, Nichols Thomas E. *Statistical parametric mapping: the analysis of functional brain images*. Elsevier; 2011.
- [57] Kasper Lars, Bollmann Steffen, Diaconescu Andreea O., et al. The PhysIO Toolbox for Modeling Physiological Noise in fMRI Data. *Journal of Neuroscience Methods*. 2017;276:56–72.
- [58] Moeller Steen, Ramanna Sudhir, Lenglet Christophe, et al. Self-navigation for 3D multishot EPI with data-reference. *Magnetic Resonance in Medicine*. 2020;84(4):1747–1762. Number: 4.

## Tables

Table 1: Mean tSNR values over all six subjects are given after realignment for different anatomies. The rightmost column shows *Whole brain* before realignment for reference. Overall, PEERS improves tSNR more substantially than PMC. However, note that no motion instructions were given and that the study included only healthy, experienced volunteers. Abbreviations: GM, gray matter; WM, white matter; CSF, cerebrospinal fluid.

Method	GM	WM	CSF	Whole brain	Whole brain not aligned
PMC off	56.69	62.86	40.41	56.10	38.50
PMC on	57.10	61.48	41.66	56.21	54.44
PMC off - PEERS	59.73	66.82	42.37	59.53	41.55
PMC on - PEERS	60.75	66.96	44.65	60.51	59.36

## Figures

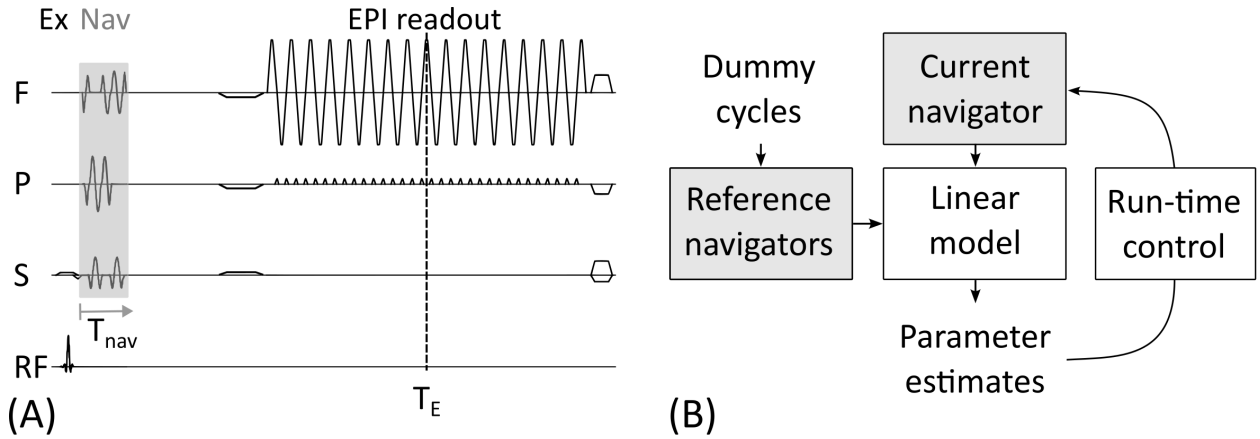


Figure 1: Servo navigation for segmented 3D EPI. (A) Sequence diagram. (B) Servo navigation overview. A 3D orbital navigator (Nav) with adaptable duration  $T_{nav}$  is inserted between excitation (EX) and EPI readout. After some dummy cycles, reference navigators are acquired on the fly to calibrate a linear model for motion and field parameter estimation. The parameters are used for run-time scan geometry control closing a feedback loop for updated linear parameter estimation.

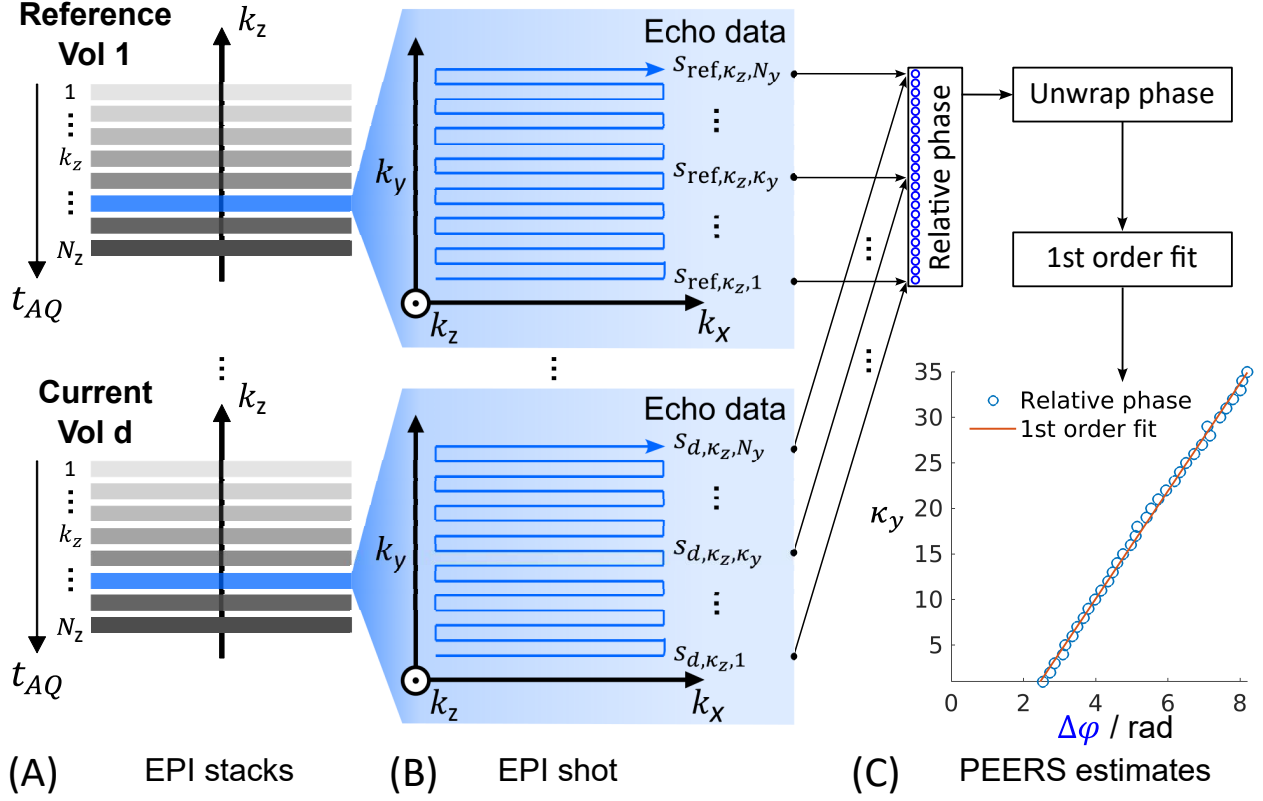


Figure 2: Phase equalization exploiting repeated shots (PEERS) overview. (A) Shots from the first EPI stack (volume) serve as a reference for phase equalization of subsequent shots. (B) For any EPI shot from a volume  $d$ , relative phases are calculated echo-by-echo by scalar products of each echo signal  $s_{d, \kappa_z, \kappa_y}$  with its respective reference peer.  $\kappa_y$  and  $\kappa_z$  are the phase and slice encoding indices, respectively. (C) The phases are unwrapped along the EPI echo train ( $\kappa_y$ ) followed by a first-order fit. Frequency and phase parameters are extracted from the slope and offset of the fit.

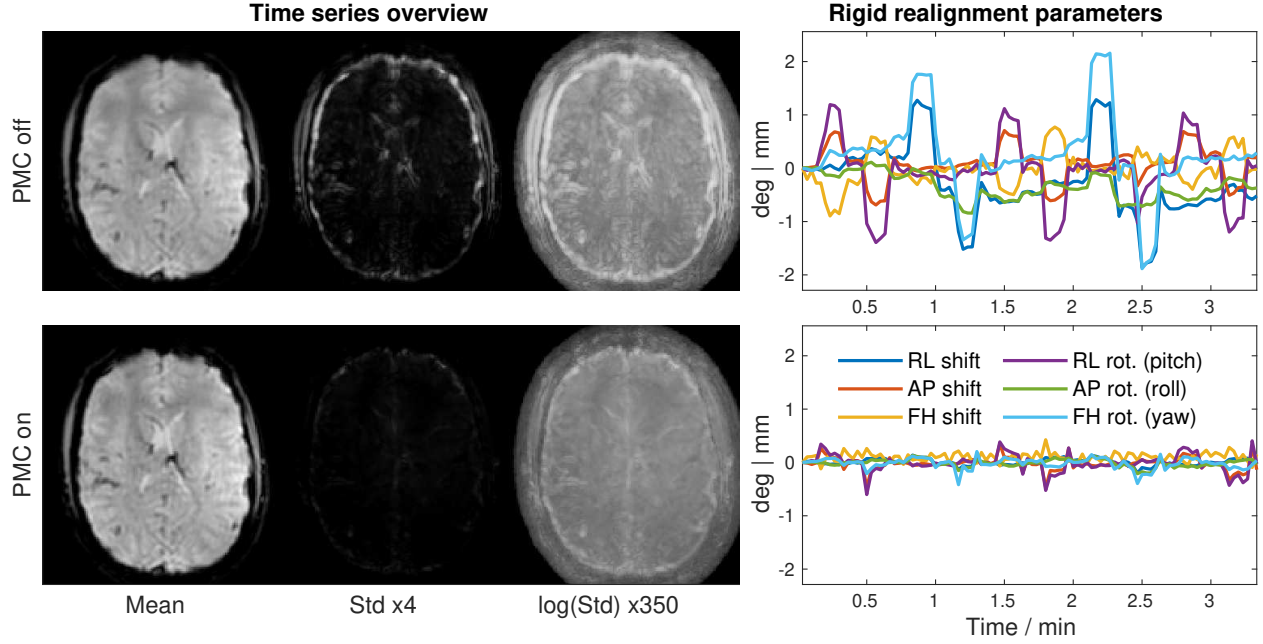


Figure 3: In-vivo example with instructed motion comparing *PMC off* and *PMC on*. (Left): Mean and standard deviation (std) of the voxel time series. (Right): realignment parameters. For *PMC off*, the mean image is blurred and the std shows strong edge enhancement and choppy patterns in the logarithmic standard deviation, which are clearly mitigated by *PMC on*. The realignment parameters for *PMC off* show the instructed motion pattern, while being close to zero for *PMC on* due to effective run-time motion correction.

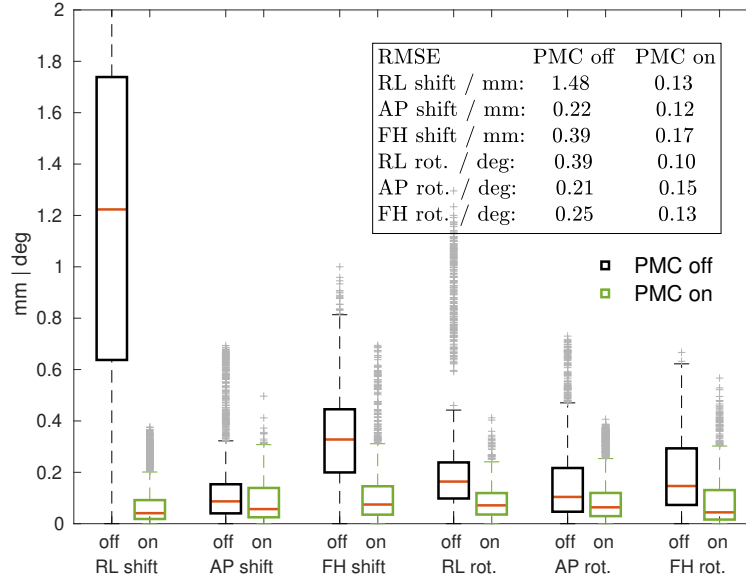


Figure 4: Volume realignment statistics for all in-vivo subjects without instructed motion comparing *PMC off* (black boxes) and *PMC on* (green boxes). Boxplots for shifts along RL, AP, and FH are shown, as well as the respective rotations. A table of parameter RMSE values is included. Motion is consistently reduced by the PMC for all parameters. The RL shift (phase encoding direction), which includes both subject motion and EPI shifting from frequency drift, shows the strongest reduction.



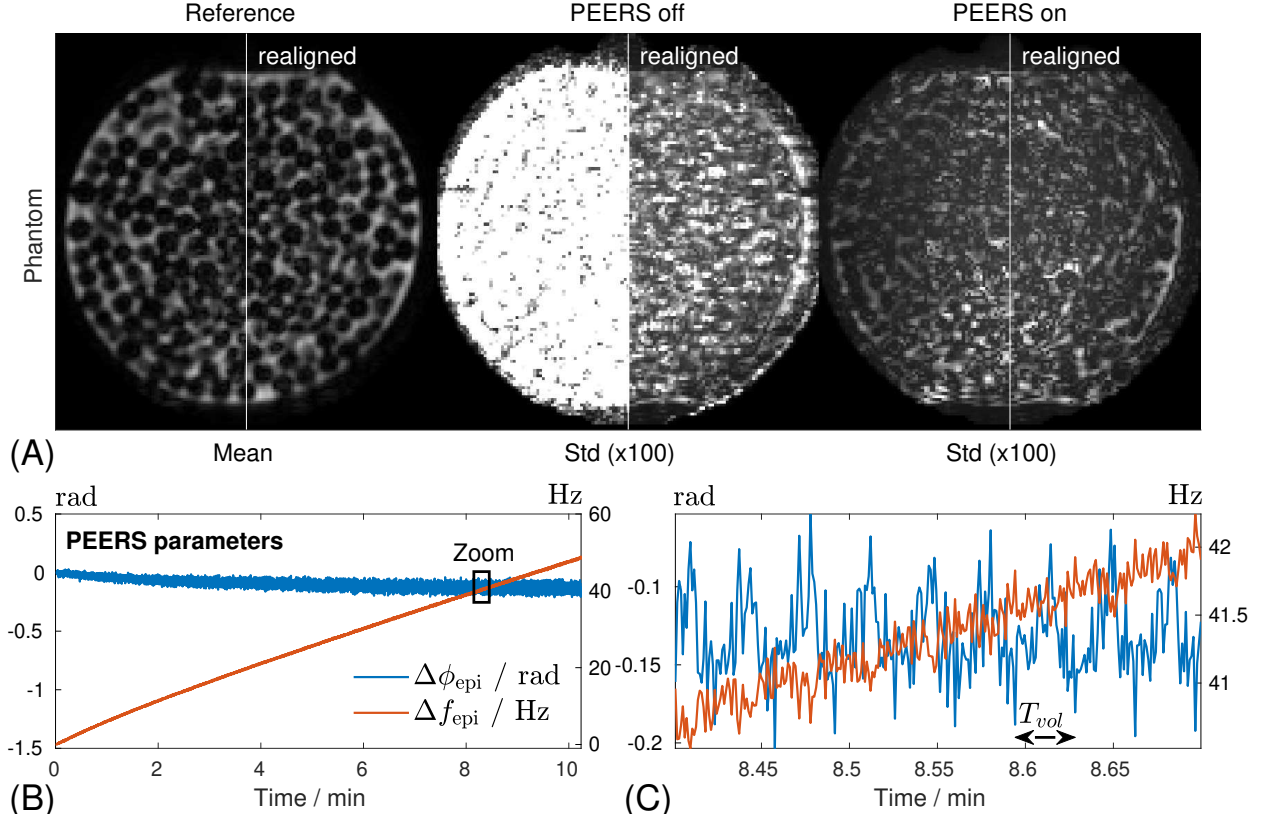


Figure 5: PEERS correction of voxel times series in a phantom scan without PMC. (A): Mean and standard deviations (std) without and with PEERS. Each image is split by half showing the image before and after realignment. (B): Phase  $\Delta\phi_{\text{epi}}$  and frequency  $\Delta f_{\text{epi}} = \Delta\omega_{\text{epi}}/(2\pi)$  estimated by PEERS. (C): Zoom into (B). Frequency drift is the main cause for standard deviation in the time series, which is reduced by realignment for PEERS off. PEERS captures the frequency drift well (B) and further improves volume consistency by intra-volume phase correction. Repetitive patterns with  $T_{\text{vol}}$ -period are visible in (C).

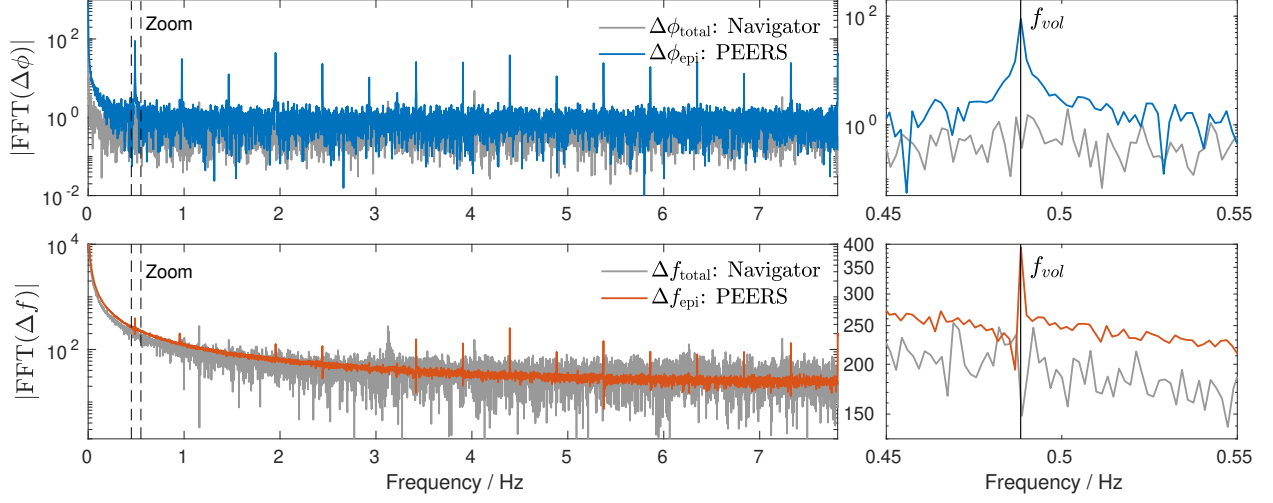


Figure 6: PEERS parameter spectra for phantom scan without PMC in Figure 5. (Top row): Phase power spectrum. (Bottom row): Frequency power spectrum. Both spectra are compared to the respective navigator parameter spectra. Zooms on the volume frequency  $f_{vol}$  are provided on the right. Dirac-combs with  $f_{vol}$ -spacing are visible for PEERS but not for the navigator, indicating that the EPI signal is subject to slice encoding-related gradient characteristics unseen by the navigator and corrected by PEERS.

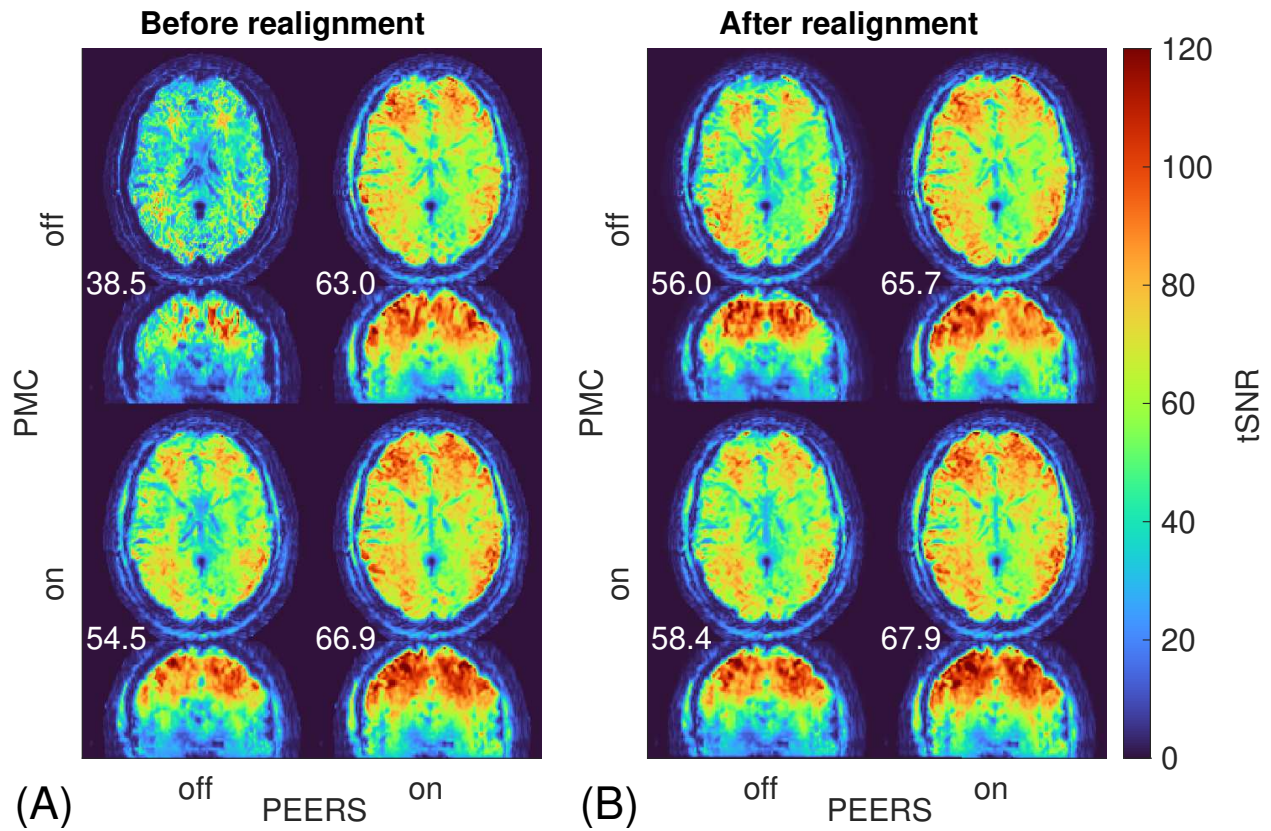


Figure 7: In-vivo tSNR example of one subject without instructed motion comparing the performance of PMC and PEERS. (A) Before realignment. (B) After Realignment. Mean tSNR values for whole brain are given in the images. Without any of the three corrections (top left) tSNR is lowest mainly due to frequency drift. Both PMC and PEERS improve tSNR individually, but are most effective together. Realignment further contributes a small tSNR improvement.

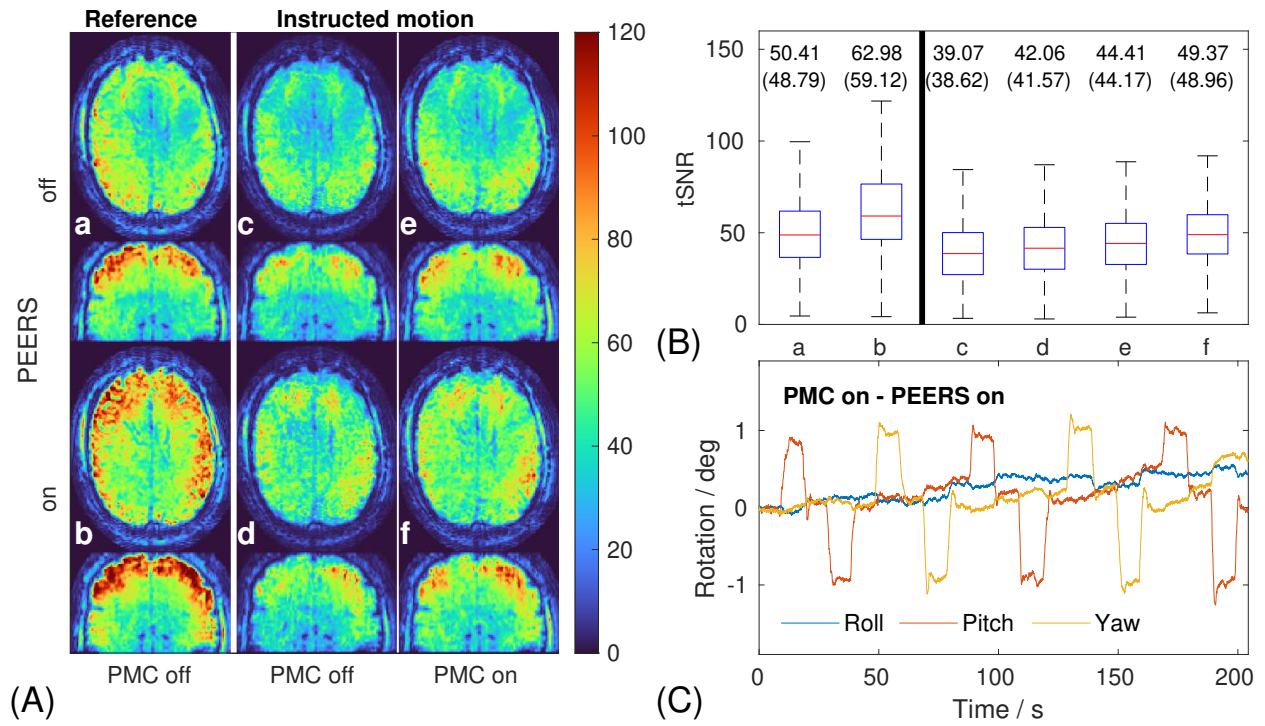


Figure 8: In-vivo tSNR example with instructed motion comparing the performance of PMC and PEERS after realignment. (A) tSNR images without (a-b) and with (c-f) motion. (B) Associated tSNR boxplots with mean (median) values. (C) Navigator-based rotation parameters for *PMC on*. The boxplots show a clear tSNR reduction by motion without PMC and PEERS (c). With motion, the PMC contributes higher tSNR gains than PEERS, although both consistently improve tSNR. Nevertheless, even combination of PMC and PEERS stay below the motion-free tSNR with PEERS.

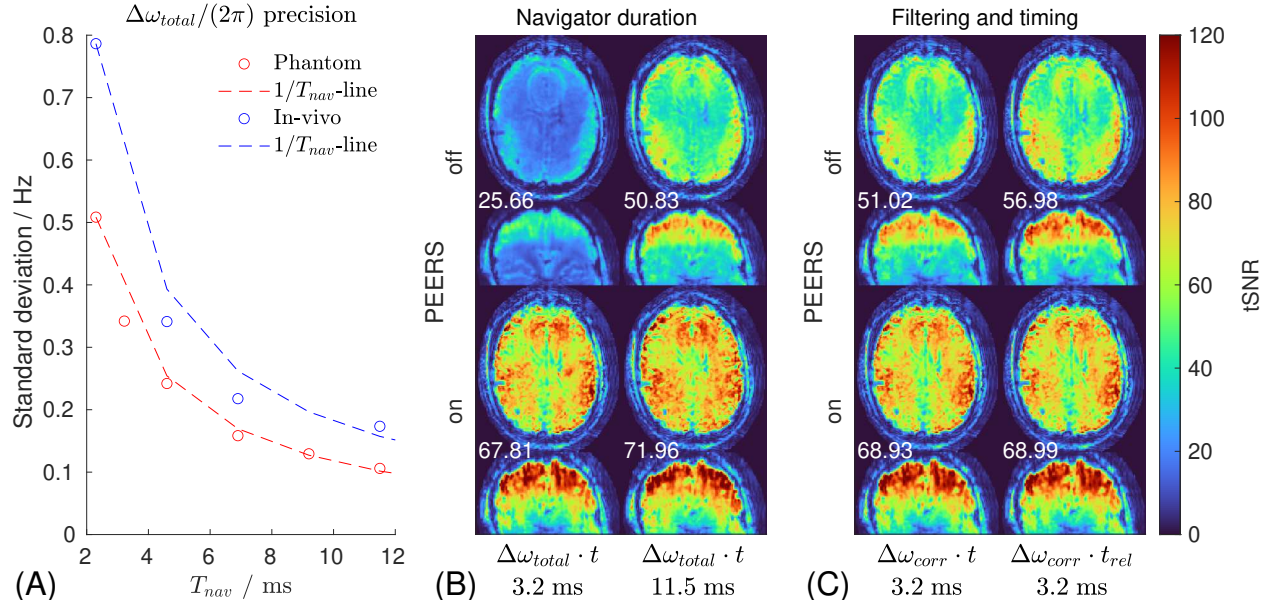


Figure 9: Considerations regarding navigator- and EPI-based frequency estimates for image correction. (A) Frequency precision for different navigator durations  $T_{nav}$ . (B) tSNR impact of PEERS and  $T_{nav}$ . (C) tSNR impact of filtering and relative timing  $t_{rel}$ . The phase correction type and  $T_{nav}$  are indicated below the images. Phase correction is either without ( $\Delta\omega_{total}$ ) or with ( $\Delta\omega_{corr}$ ) filtering and with absolute ( $t$ ) or relative ( $t_{rel}$ ) timing. Long navigators, filtering and relative timing all improve navigator frequency corrections. EPI-based PEERS corrections perform better but require a repetitive sequence structure.